Anisotropic step etching and etch instabilities during cathodic corrosion on platinum

Trindell, J.A.; Aarts, M.; Koper, M.T.M.

Citation
Trindell, J. A., Aarts, M., & Koper, M. T. M. (2025). Anisotropic step etching and etch instabilities during cathodic corrosion on platinum. *Journal Of Physical Chemistry C*, *129*(43), 19389-19395. doi:10.1021/acs.jpcc.5c05071

Version:	Publisher's Version
License:	Creative Commons CC BY 4.0 license
Downloaded from:	https://hdl.handle.net/1887/4283088

Note: To cite this publication please use the final published version (if applicable).

THE JOURNAL OF PHYSICAL CHEMISTRY C
A JOURNAL OF THE AMERICAN CHEMICAL SOCIETY

Open Access
This article is licensed under CC-BY 4.0

pubs.acs.org/JPCC
Article

Anisotropic Step Etching and Etch Instabilities during Cathodic Corrosion on Platinum

Published as part of The Journal of Physical Chemistry C special issue "Degradation of Electrochemical Materials in Energy Conversion and Storage".

Jamie A. Trindell,[†] Mark Aarts,[†] and Marc T. M. Koper*

Cite This: J. Phys. Chem. C 2025, 129, 19389−19395

Read Online

ACCESS | Metrics & More | Article Recommendations | Supporting Information

ABSTRACT: The process of cathodic corrosion on platinum electrodes in aqueous environments is inevitably obscured by concurrent hydrogen evolution. Insights into the corrosion mechanism and progression are, therefore, most straightforwardly obtained through postcorrosion characterization. In this work, we use ex situ microscopy to evaluate the progression of etch pits on (111)- and (100)-facets of single-crystal platinum electrodes. While the corrosion process has previously been shown to be anisotropic, we observe that etching mainly occurs at undercoordinated step edges rather than into the plane. Such a dependence on the local energetics of the platinum surface atoms is also evident by a pit nucleation barrier on the (100)-facet, where nucleation occurs preferentially on dislocations in the crystal lattice. On the (100)-facet, we also observe an etching instability that results in both rapid downward etching and material redeposition. Through the observed nucleation-and-growth nature of the etch pits in cathodic corrosion, we envision that the etching (and subsequent redeposition) process can be tailored through control over the surface energetics, similar to methods known from electrodeposition.

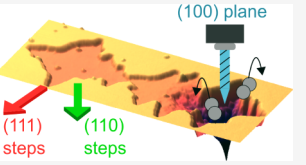

Downloaded via 86.84.197.165 on November 19, 2025 at 11:13:19 (UTC).
See https://pubs.acs.org/sharingguidelines for options on how to legitimately share published articles.

INTRODUCTION

Cathodic corrosion of platinum in aqueous environments concerns the counterintuitive dissolution of the metal electrode at cathodic potentials.[1] Studying cathodic corrosion is challenging, however, as the process requires potentials at which the electrochemical reduction of water occurs simultaneously.[2] This competing hydrogen evolution reaction results in low faradaic efficiencies for the corrosion process, such that the transient electrochemical signal holds little information about the etching process.[3,4] The recent observation of cathodic corrosion on copper electrodes under CO_2 reduction conditions[5,6] has given an impulse to interest in the cathodic corrosion process, on copper as well as other electrode materials.[7,8] In fact, recent works have managed to obtain information on the cathodic dissolution in-operando,[9,10] but in all cases the vigorous H_2 evolution at potentials relevant for cathodic corrosion severely complicates the use of in situ techniques. The underlying mechanism of atomic etching under these conditions therefore remains elusive,[11,12] even though there is recent spectroscopic evidence for the formation of platinum hydrides under severe cathodic corrosion conditions.[13]

On platinum, previous studies of cathodic corrosion have mainly focused on the resulting electrode morphology after corrosion. It was observed that the process is anisotropic,[14] indicating that the local surface energy of the platinum atoms determines the kinetics of the etching process to a large degree. Specifically, our group has previously used ex situ scanning electron microscopy (SEM) analysis to investigate the formation of triangular versus square-shaped etch pits on Pt(111)- and (100)-planes, respectively, in 10 M NaOH.[15] Furthermore, the solvent[16] as well as the concentration and identity of irreducible electrolyte cations[17−19] also influence the structural evolution of the electrode surface. While corrosion occurs most readily in highly alkaline electrolytes (e.g., 10 M NaOH), the shape of etch pits observed on platinum appears to be largely independent of the bulk electrolyte pH. Specifically, corrosion has also been reported to occur on Pt(111) in acidic media (pH = 1), and the resulting pit shape (i.e., triangular pits)[20] is the same as in all reports in alkaline media. A likely explanation is that, due to the vigorous hydrogen evolution, the local pH is very alkaline. Such local pH effects could affect the observed corrosion process, regardless of the bulk pH.[1]

The cathodic corrosion of platinum is typically regarded to favor the formation of facets with (100) orientation based on cyclic voltammetry (CV) of the corrosion products (i.e., nanoparticles)[21,22] as well as the corroded electrode.[14] In contrast, another study concluded that the etching order was

Received: July 21, 2025
Revised: October 10, 2025
Accepted: October 10, 2025
Published: October 22, 2025

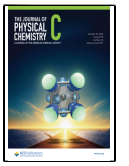

© 2025 The Authors. Published by American Chemical Society

(111) >; (100) >; (110) based on qualitative evaluation of the two-dimensional evolution of the footprint area using SEM,[15] which is therefore expected to expose (110)-planes instead. These experiments have been typically conducted at highly negative potentials or in concentrated electrolytes (i.e., 10 M NaOH). Such harsh conditions result in rapid corrosion, making it difficult to carefully track the progression of individual pits over time. Another major limitation is that SEM does not provide data on the depth or volume of the etch pits. This type of quantitative information is needed to further understand cathodic corrosion on Pt electrodes.

In this work we evaluate the cathodic corrosion of single-crystal platinum electrodes using *ex situ* microscopy in a comparatively mildly corroding 1 M NaOH to investigate: (i) pit orientation and determine anisotropic etching patterns; (ii) compare etching into the plane versus along step edges; and (iii) use identical-location AFM to track the nucleation and growth of pits on the (100)-facet. Performing corrosion under mild conditions allows us to track the nucleation-and-growth process of individual corrosion pits. Specifically, we use atomic force microscopy (AFM) and SEM to reveal the evolution of the three-dimensional morphology of cathodic corrosion pits in the (111)- and (100)-crystal facets. We observe, first, that corrosion progresses primarily through etching of the (111)-, and (110)-steps at the pit boundaries with only mild etching into the plane. Second, that pits nucleate on the (111)-facet much more readily than on the (100)-facet, as evidenced by the pit density. Finally, we use identical location AFM to track the pit evolution over time on the (100)-plane. We observe that pits suffer from an etching instability (i.e., a type of self-accelerated etching mechanism), which results in the rapid formation of a deep hole in its center accompanied by redeposition of Pt onto the pit wall. Continued material redeposition results in a rounded pit opening at longer corrosion times, with downward etching being limited to ∼200 nm. This process does not appear to be anisotropic and does not result in a faceted side wall, as was expected based on previous reports. Finally, we observe that the increased nucleation barrier on the (100)-facet results in drastically favoring pit nucleation at defects or dislocations of the underlying crystal lattice.

Taken together, our experiments show that cathodic corrosion pits follow a nucleation-and-growth process, with nucleation promoted by inhomogeneities or defects in the underlying crystal, and the growth progressing mainly through the etching of steps rather than the terraces. On the (100)-facet this process can also be subject to a self-accelerated etching mechanism that does not appear to be specifically anisotropic.

METHODS

Single-Crystal Electrodes. Single-crystal bead electrodes were fabricated by melting the end of a platinum wire (Goodfellow, 1 mm diameter, 99.998%) in a hydrogen (H_2, 99.999%, Lindegas) oxygen (O_2, 99.999%, Lindegas) flame, with a coaxial argon (Ar) gas flow (99.999%, Lindegas) protecting the flame. The molten bead is slowly crystallized by retracting the flame with a motorized stage. The bead is cooled under Ar flow for 5 min after completing the crystallization. The (100) platinum single-crystal disk electrode (Figure 5) was obtained from MaTeck.

Microscopy. AFM measurements were conducted on a JPK NanoWizard 4 in either AC mode or QI-mode, using OPUS 160AC-NG and OPUS 240AC-NG probes with a nominal radius <7 nm. Relevant for the imaging of pits due to the maximum measurable slope, these probes have half cone angles of 0° (front), 35° (back), and <9° (sides). SEM images were obtained using the T2 detector on an Apreo2 (Thermo Scientific) with 0.8 nA at 15 kV acceleration voltage (Figure 5a) and 0.1 nA at 2 kV acceleration voltage (Figure 5b,c). Measurements were executed *ex situ* due to the difficulty of imaging the surface during vigorous hydrogen evolution, as well as the incompatibility of the glass AFM holder with the alkaline electrolyte.

Electrochemistry. Electrochemical experiments were conducted in a homemade perfluoroalkoxy cell (PFA) resistant to the alkaline electrolyte. The cells were cleaned by overnight soaking in an acidified potassium permanganate solution containing 1 g/L $KMnO_4$, (>99%, ACS reagent, Emsure) with 0.5 M H_2SO_4 (98%, ACS reagent, Sigma-Aldrich). The cell was then immersed in dilute piranha solution (35% H_2O_2, Merck and H_2SO_4, 98%, ACS reagent, Sigma-Aldrich) to remove residues of manganese oxide and permanganate anions, followed by boiling at least 3 times in ultrapure water (Milli-Q, resistivity > 18.2 MΩ cm). Experiments were conducted using a BioLogic VSP-300 potentiostat, with a platinum counter electrode and a RHE reference electrode (Hydroflex, Gaskatel). Cathodic corrosion was conducted using 30% NaOH (10 M, Suprapur, Merck) diluted to 1 M with ultrapure water. Prior to cathodic corrosion the electrolyte was purged with Ar (99.999%, Lindegas), and Ar was flown over the solution during electrochemical experiments.

To study pit formation on the (111) surface, platinum bead electrodes were corroded potentiostatically for 1 or 3 min at −0.65 V vs RHE (85% IR compensated, Figure S1). For the (100) surfaces, beads were corroded galvanostatically at −500 mA (bead surface area approximately 0.1 cm^2).

RESULTS AND DISCUSSION

Shape Evolution for Anisotropic Etching on the (111) Facet of Pt Beads. Cathodic corrosion experiments were conducted potentiostatically in a 1 M NaOH electrolyte, with applied potential and duration chosen empirically to result in a degree of corrosion that allowed for the identification of individual etch pits. The corrosion process was done in a three-electrode cell using a reversible hydrogen electrode (RHE) as the reference and a platinum counter electrode. As a working electrode, single-crystalline platinum bead electrodes were used. These electrodes were fabricated by melting of a platinum wire, followed by slow crystallization (experimental details outlined in Methods section).[23] Figure 1a shows a scanning electron microscopy (SEM) image of such a bead after fabrication. As previously reported, these Pt bead single crystals are not perfectly spherical and contain faceted regions of interest. The three low index planes are highlighted (100 = blue, 110 = green, 111 = red), where the beads orient with the (100) direction oriented nominally toward the bottom, and the (111)-facets are readily visible. These low-index planes are connected over the curved surface of the spherical bead corresponding to the outline of the stereographic triangle.[23] The inset of Figure 1a shows an SEM image of the (111)-plane after cathodic corrosion, displaying the characteristic triangular etching pattern that we have previously reported on both (111)-facets of Pt beads and Pt(111) single crystals.[14,15,20] Importantly, these triangles are oriented in the same direction in all our experiments.

https://doi.org/10.1021/acs.jpcc.5c05071
J. Phys. Chem. C 2025, 129, 19389−19395

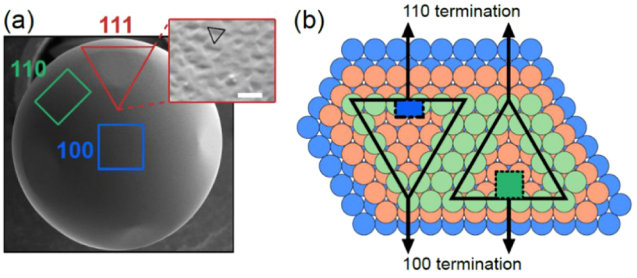

Figure 1. (a) SEM image of a platinum bead, the position of representative low index facets is highlighted. Inset: Typical morphology of the (111)-facet after mild cathodic corrosion. The black triangle outlines one of the pits. The scalebar is 150 nm. (b) Ball model representation of the two possible pit orientations that yield a triangular shape. Colors of the atoms indicate different layers. The pits result in either (100) oriented sidewalls (blue square, left), or (110) oriented sidewalls (green square, right). In all our experiments the triangles point toward the (100)-facets, i.e., the left pit.

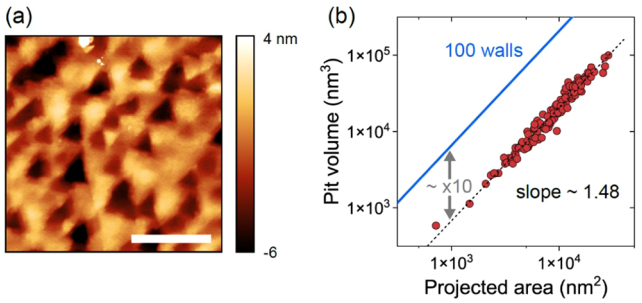

Figure 2. (a) AFM topography of the corroded (111)-facet, where individual pits can still be distinguished. The scale bar is 400 nm. (b) Pit volume vs projected area on a log−log scale, where each data point represents a single etch pit. The dashed line is a linear fit to the data with slope ∼1.48, indicating that the aspect ratio is maintained for all considered pits. The solid blue line indicates the expected volume for a specific projected area considering (100) sidewalls, i.e., making an angle of 54.7°. The data is significantly offset to lower volumes, by a factor ∼10, indicating that the pits are much more shallow.

While the triangular shape follows the symmetry of the (111)-orientation of the face-centered-cubic crystal, we can deduce the etching direction from the bead geometry, as illustrated in Figure 1b. We observe that the etch pits always point toward the (100)-termination of the bead (left side in Figure 1b), with the walls directed toward the (110)-termination. This orientation actually results in (100)-step sites (blue square on the left side) being exposed on the pit walls. Alternatively, triangles with corners pointing toward the (110)-termination have (111)/(110)-steps exposed on the walls (green square on the right side). Notably, we have not observed this orientation of the triangular shaped etch pits on the Pt bead electrodes.

This observed orientation of the triangles, with (100)-stepped walls, is in line with the previously proposed shape based on CV analysis,[14] and indicates that the cathodic etching rate is higher for the (111)/(110)-steps than the (100)-steps. Specifically, through CV analysis of the electrode before and after corrosion experiments, the (100) peaks for hydrogen underpotential deposition were observed to build-in with increasing corrosion time. In the current experiments on spherical single-crystal beads the CVs are convoluted over all facets. Therefore, since CV analysis has been extensively studied for these Pt beads and because it is difficult to conclude the origin of the changes in the (100) peak, CVs are not reported in this manuscript. Instead the reader is directed to our previous studies for more details.[14,15,18,20]

While SEM provides insight into the crystallographic direction of etching along the perimeter of the pits, we used atomic force microscopy (AFM) to further track the progression of the 3-dimensional morphology of the pit and differentiate between this step etching along the perimeter and the downward etching into the (111)-plane. Figure 2a shows an AFM topography image of the corroded (111)-plane, where the process was stopped after different corrosion times (see Methods) before severe overlap of the etch pits occurred.[20] From the AFM images, we obtain both projected area of the pit and the resulting pit volume, which is used to quantitatively evaluate the evolution of the pit shape, using the analysis by Guo and Searson.[24,25]

Briefly, we assume that all islands grow independently prior to coalescence and that their size is determined by the growth time. If growth is constant in every direction over time (t), the projected area of the pit scales with t^2 and the pit volume with t^3, yielding a slope of 1.5 when plotting volume vs area on a log−log plot. This is shown in Figure 2b, considering the footprint and volume of individual pits (133 pits, Figure S1). This *slope* holds information about the relative scaling of the growth directions, or how well the shape is maintained, while the *position* of the curve is determined by the actual shape, or aspect ratio, of the pit.[26]

We observe that the slope in the log−log representation is ∼1.5, indicating that the shape of the pits is maintained over the projected area range (yielding sides of ∼40 nm to ∼250 nm, considering equilateral triangles). However, when comparing the pit volume with that of a theoretical pit with 100 sidewalls (calculation in S2) as expected from the CV,[14] we observe that the position of the curve is strongly offset toward lower volumes, by a factor ∼10. Taken together, we conclude that while the *ratio* between the step etching (increasing pit footprint) and the downward (111)-plane etching is maintained, the etching *rate* into the (111)-plane is modest. The largest pits in Figure 2b have a depth <10 nm, such that the etch rate at the corners is estimated to be ∼25 times faster than the z-direction into the plane (Figure S3). While similar to the qualitative description by Chen and Koper,[20] this conclusion is somewhat surprising considering that the (111)-facet was previously considered to corrode the fastest.[15] However, these earlier conclusions were mainly supported by qualitative observations of higher pit density and apparent surface roughening on (111)- versus (100)- and (110)-facets during corrosion experiments. In this report, we perform a more detailed quantitative analysis which provides additional considerations to differentiate between rate of etching into a plane and step-etching. In fact, such a step etching process is very similar to the wet etching of silicon where the (111)-plane is the slowest etching plane,[27] and was also proposed recently for the electrochemical pitting dissolution of silver.[28]

Tracking Pit Nucleation and Growth on the (100) Facet of Pt Beads. We now turn our attention to the (100)-facet, which displays square-shaped etch pits. In comparison to the (111)-facet, pit nucleation on the (100)-facet is more sparse with a lower density of pits per surface area. Second, anisotropic etching with a preferred pit orientation is also observed,[15] which is shown in Figure 3a to result in the exposure of the (110)-orientation on the side wall (green

https://doi.org/10.1021/acs.jpcc.5c05071
J. Phys. Chem. C 2025, 129, 19389−19395

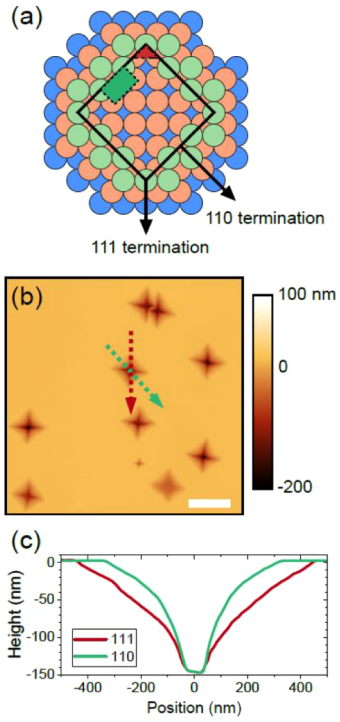

Figure 3. (a) Ball model representation analogous to Figure 1a for the etch pits observed in the (100)-plane. This results in (110) oriented sidewalls (green square) with (111)-steps in the corners (red triangle). (b) AFM topography image of etch pits in the (100)-facet. The scale bar is 1 μm. (c) Line profiles indicated in (b) along the (111), red, and (110), green, directions. The profile is concave, with a shallow sidewall which transitions to a steep profile at the deepest part of the pit.

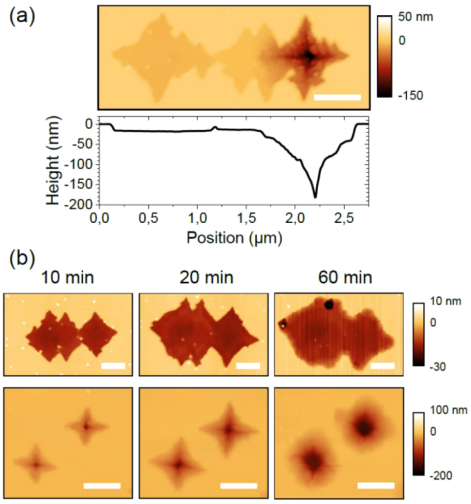

Figure 4. (a) AFM topography image of multiple pits that nucleated in a line, where only one displayed the etching instability. The line profile is taken along the center of image. The stable pits are shallow with a flat base. The unstable pit is much deeper, and shows a roughened mouth, attributed to material redeposition. The scalebar is 500 nm. (b) Identical location AFM topography images after (left) 10 min, (middle) 20 min, and (right) 60 min of cathodic corrosion. The top row shows stable etch pits that mainly grow laterally over time. The bottom row shows unstable etch pits. These deep pits etch down slightly over time, but mainly widen, resulting in a flat base. The widening still removes significant amounts of material, which is likely to result in the smooth and rounded mouth of the pits through redeposition. The scalebars are 500 nm.

square), and the (111)-orientation in the corners (red triangle). While these observations are in agreement with previous experiments using SEM analysis, they are not explained by typical CV characterization of the corroded surface.[14] High-resolution AFM analysis on these pits has not been reported until now.

Figure 3b,c showa an AFM topography image and associated line profiles, respectively, for a representative etch pit. In general, the pits are much deeper than on the (111)-facet, forming a concave shape with a shallow mouth and steep hole in the center. This indicates a sudden enhanced etch rate at the center of the pit, compared to the rest of the plane, implying a self-enhancing process.

Interestingly, while most pits suffer from an instability resulting in a highly enhanced local etching rate and yielding a narrow and deep hole, not all pits on the (100)-facet exhibit this type of etching profile. Specifically, we identified two different types of etch pits on the (100)-facet: (i) "stable" and shallow etch pits (depth < 20 nm) and (ii) "unstable" etch pits with locally accelerated downward etching (depth > 50 nm). It should be noted that under the studied conditions, the vast majority of observed pits fall into the unstable category, as shown in S4. These two different types of etch pits on the (100)-facet are more clearly visible in Figure 4a, where multiple pits have nucleated next to each other. The horizontal line profile along the center of the image shows that the pits in the (100)-facet also have a modest depth (~20 nm) compared to the radius (~400 nm), i.e., yielding a similar ratio of 20 as found on the (111)-plane. However, the occurrence of a sudden enhanced etch rate at the center of the pit, compared to the rest of the plane, results in a sharp and deep (~180 nm) hole in the middle of the far-right pit. Furthermore, the mouth of this opening roughens significantly, yielding the concave profile for the sidewalls, which we attribute to redeposition of material before it leaves the pit. In fact, local redeposition decouples the volume of the pit from its footprint area on the electrode surface, such that we cannot use the same analysis from Figure 2b on the (100)-facet.

For stable pits the (111)-step sites have a slightly higher etching rate than the (110)-step sites, resulting in large, low aspect ratio pits, with a concave perimeter.[15] It is worth mentioning that while this perimeter of the pit appears very sharp, the slope of the sidewalls is ~30° in the presented images, in contrast to the (100)-type sides (i.e., 90°) proposed based on CV analysis.[14] Due to this previous data, we anticipated the appearance of faceted [i.e., (100), (111), or (110)] sidewalls indicative of slow-etching planes. The fact that these are not observed is attributed to the much faster etching at the surface steps compared to etching into the plane. such that the facets do not build in.

This shape evolution for the different type of pits (i.e., stable versus unstable) over total corrosion time was analyzed using identical-location AFM. Specifically, corrosion experiments in 1 M NaOH were conducted by holding the Pt bead at −500 mA and performing AFM imaging of the (100)-facet after 10, 20, and 60 min, respectively. Performing the corrosion experiments under constant current, instead of constant potential, allows for the decoupling of variation in the current and the observed corrosion. This is relevant because, over the course of an experiment, an increasing current is measured at constant potential for the cathodically corroded surface,

https://doi.org/10.1021/acs.jpcc.5c05071
J. Phys. Chem. C 2025, 129, 19389−19395

possibly due to an increased number of reactive sites. By corroding at a constant current, we ensure that changes over time are not due to this increasing current density. In any case, it seems that there is no real difference between potentiostatic versus galvanostatic control in the overall corrosion process. This is supported by the fact that the pit shape reported here for Pt(100) is consistent with prior literature,[14,15] where the shapes dictated by the underlying crystal-structure are always the same.

Figure 4b shows the AFM topography images with increasing duration of the cathodic corrosion process from 10 to 20 to 60 min. Indeed we observe the two aforementioned behavior of either modest downward etching or locally accelerated etching for the evolution of the pits over time. For the stable etch pits (top row), pit depth is limited to ∼20 nm for all etching times, while the diameter gradually increases over time. Strikingly, two deeper pits appear at the corners after the longest corrosion time. The bottom row displays the evolution of two unstable etch pits. Here too, the footprint gradually increases over time. However, this is accompanied by significant material removal from the bottom of the pit, which appears to round and smoothen the mouth of the pit. This is mainly due to broadening of the base, with further downward etching being limited at longer times (from ∼130 nm to ∼160 nm between 10 and 60 min).[15]

We can rationalize the deep etching followed by material redeposition by drawing a comparison to previous insights of anodic corrosion. In anodic corrosion and in the absence of a passivating film, as is expected to be the case on the platinum electrodes, sustained pit growth is typically attributed to local creation of an aggressive corrosion environment. This is maintained by mass-transport limitations of the active components, such as creating low local pH and enhancing migration of aggressive anions.[29] Analogously, in the cathodic corrosion process this could be attributed to increasing local pH by OH^- generation through water reduction, and enhanced migration of cations toward the bottom of the pit maintaining electroneutrality, conditions that are known to promote cathodic corrosion.[3] Furthermore, we attribute the roughening of the mouth of the pit to material redeposition, which can be compared to salt film formation in anodic corrosion due to local supersaturation of the corroding metal.[29] In the cathodic process, the observation of similar redeposition during corrosion on gold wires has also been attributed to a local increased concentration of the dissolving metal. This occurred in particular following initial pitting, resulting in recrystallization at the surface and the nucleation of faceted nanoparticles.[17] Interestingly, on both platinum[3] and gold electrodes,[18,19] the shape of nanoparticles and the degree of redeposition was found to be dependent on the concentration and identity of the cation in the supporting electrolyte. In fact, such a redeposition process could then result in a feedback loop where high etching rates result in redeposition, which in turn lead to further mass-transport restrictions, again modifying the local etching (and redeposition) environment. In our experiments, it is reasonable to consider that once an etch pit becomes deep enough, the dissolved atoms do not diffuse out of the pit before redepositing, resulting in the progressive roughening observed in Figure 4b. In fact, etching patterns that resemble diffusion-limited growth have been observed after prolonged corrosion in more aggressive electrolytes.[15]

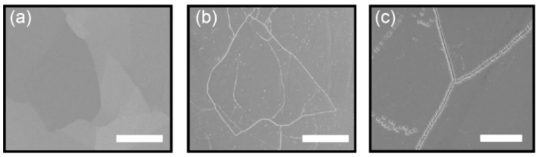

Figure 5. SEM images of a Pt(100) single-crystal disk electrode using a backscatter electron detector. (a) Before corrosion, showing regions of different contrast attributed to crystal dislocations. (b) After corrosion, where the dislocation lines are visible as white lines. (c) Higher magnification shows that these lines consist of coalesced etch pits that nucleated preferentially at the dislocations. The scale bars are 10 μm (a,b), and 2 μm (c).

The Effect of Defects on Pt(100) Disk Electrodes. Finally, we observed qualitatively that the pit nucleation density is much lower on the (100)-facet than on the (111)-facet. In this context we studied the nucleation of etch pits using a (100) single-crystal disk electrode (see Methods). Figure 5a shows an SEM image of the electrode surface prior to corrosion, using a backscattered electron detector, where the contrast difference is the expected site of a dislocation or atomic defect.[30] Figure 5b shows the same location after cathodic corrosion, where these regions of contrast change are visible as bright lines. Further magnification shows that the lines actually consist of many coalesced etch pits, as illustrated in Figure 5c, leading to the conclusion that these crystallographic defects are highly favored sites for pit nucleation. This observation is in line with those on polycrystalline Pt electrodes where corrosion occurs preferentially at grain boundaries, likely due to the higher surface energy of these regions.[18] It should be noted here that, while single-crystal electrodes should in theory be a "perfect" surface free of defects, experimentally this is often not the case and defects are often present due to scratches or even repeated thermal stress during flame-annealing.

To this point, we hypothesize that the frequent flame-annealing of the single-crystal electrodes likely does introduce a higher density of defects into the electrodes. For example, repeated flame annealing of a corroded electrode may make the Pt atoms mobile enough to begin to refill in some of the pits, but the inability of the Pt electrodes to fully "recover" to a pristine surface likely results in the types of defects observed for the Pt(100) surface. For the Pt beads, however, a pristine bead can be easily regenerated by remelting and recrystallizing, thus avoiding defects that may cause preferential nucleation. This type of "recovery" or restoration of the pristine surface of the Pt bead electrode is not possible for polished Pt single crystals. Therefore, this result of accelerated cathodic corrosion at dislocations in the crystal lattice is an important point considering the difficulty in attaining pristine, defect free surfaces of Pt electrodes.

CONCLUSIONS

Summarizing our results, we observed that pit formation during cathodic corrosion of platinum in aqueous electrolytes follows a nucleation-and-growth process. Pits readily nucleate for the (111)-plane, but further etching occurs primarily at the (111)/(100)-steps, while etching into the (111)-plane is characterized by a much lower rate. Cathodic corrosion on the (100)-plane nominally progresses in a similar way, where lateral etching of the (111)-, and (110)-steps is much faster than downward etching into the plane. However, most pits are

https://doi.org/10.1021/acs.jpcc.5c05071
J. Phys. Chem. C 2025, 129, 19389−19395

at some point subject to a self-accelerated etching instability leading to high local dissolution rates. This is likely due to mass-transport limitations in the pits creating a more aggressive corrosion environment, which then does not appear to be specifically anisotropic. Rather, this leads to roughened sidewalls due to material redeposition at the mouth of the pit. Finally, on the (100)-plane it is particularly evident that nucleation is promoted by crystal inhomogeneities providing nucleation sites, similar to the hypothesis that pit nucleation occurs at step sites on the (111)-plane.[20]

Overall, our results highlight nuances in the energetics of cathodic corrosion, where anisotropic etching occurs primarily at undercoordinated step edges. This could potentially be leveraged to direct and control the corrosion pitting (and subsequent deposition) process similarly to well-known electrodeposition schemes, such as the use of facet-stabilizing electrolytes[31] or controlled potentials.[32]

■ ASSOCIATED CONTENT

Supporting Information

The Supporting Information is available free of charge at https://pubs.acs.org/doi/10.1021/acs.jpcc.5c05071.

AFM topography images and AFM analysis of the pit shapes (PDF)

■ AUTHOR INFORMATION

Corresponding Author

Marc T. M. Koper − *Leiden Institute of Chemistry, Leiden University, Leiden 2333 CC, The Netherlands;* orcid.org/0000-0001-6777-4594; Email: m.koper@lic.leidenuniv.nl

Authors

Jamie A. Trindell − *Leiden Institute of Chemistry, Leiden University, Leiden 2333 CC, The Netherlands*

Mark Aarts − *Leiden Institute of Chemistry, Leiden University, Leiden 2333 CC, The Netherlands;* orcid.org/0000-0002-4499-9130

Complete contact information is available at: https://pubs.acs.org/10.1021/acs.jpcc.5c05071

Author Contributions

†J.A.T. and M.A. contributed equally.

Notes

The authors declare no competing financial interest.

■ ACKNOWLEDGMENTS

This work received funding support from Hitachi High-Tech Corporation. The authors would like to acknowledge useful discussions with Hitachi High-Tech. The AFM measurements were performed in the Leiden Institute of Physics AFM Facility, for which the authors acknowledge Dr. Federica Galli for training and support. We further acknowledge the support of the fine mechanical department at Leiden University and Thijs Hoogenboom for manufacturing the electrochemical cell.

■ REFERENCES

(1) Yanson, A. I.; Rodriguez, P.; Garcia-Araez, N.; Mom, R. V.; Tichelaar, F. D.; Koper, M. T. M. Cathodic Corrosion: A Quick, Clean, and Versatile Method for the Synthesis of Metallic Nanoparticles. *Angew. Chem., Int. Ed.* **2011**, *50*, 6346−6350.

(2) Hersbach, T. J. P.; Koper, M. T. M. Cathodic corrosion: 21st century insights into a 19th century phenomenon. *Curr. Opin. Electrochem.* **2021**, *26*, 100653.

(3) Yanson, A. I.; Antonov, P. V.; Rodriguez, P.; Koper, M. T. M. Influence of the electrolyte concentration on the size and shape of platinum nanoparticles synthesized by cathodic corrosion. *Electrochim. Acta* **2013**, *112*, 913−918.

(4) Scharifker, B.; Hills, G. Theoretical and experimental studies of multiple nucleation. *Electrochim. Acta* **1983**, *28*, 879−889.

(5) Liu, S.; Li, Y.; Wang, D.; Xi, S.; Xu, H.; Wang, Y.; Li, X.; Zang, W.; Liu, W.; Su, M.; et al. Alkali cation-induced cathodic corrosion in Cu electrocatalysts. *Nat. Commun.* **2024**, *15* (1), 6092.

(6) Sarker, H. P.; Goswami, A.; Tang, M. T.; Abild-Pedersen, F. From Micro-environments to Macroscopic Effects: How the Alkaline Hydrogen Evolution Reaction Drives Cu Cathodic Corrosion. *ACS Catal.* **2025**, *15*, 8676−8690.

(7) Wei, Q.; Tang, M.; Shi, H.; Zhu, H.; Du, K.; Wang, D. Corrosion Behavior and Mechanism of Nickel as a Hydrogen Evolution Electrode Under High Alkalinity and Temperature. *J. Electrochem. Soc.* **2024**, *171*, 121505.

(8) Lee, S. H.; Avilés Acosta, J. E.; Lee, D.; Larson, D. M.; Li, H.; Chen, J.; Lee, J.; Erdem, E.; Lee, D. U.; Blair, S. J.; et al. Structural Transformation and Degradation of Cu Oxide Nanocatalysts during Electrochemical CO 2 Reduction. *J. Am. Chem. Soc.* **2025**, *147*, 6536−6548.

(9) Yang, Y.; Shao, Y.-T.; Lu, X.; Yang, Y.; Ko, H.-Y.; DiStasio, R. A.; DiSalvo, F. J.; Muller, D. A.; Abruña, H. D. Elucidating Cathodic Corrosion Mechanisms with Operando Electrochemical Transmission Electron Microscopy. *J. Am. Chem. Soc.* **2022**, *144*, 15698−15708.

(10) Yan, K.; Lee, S. W.; Yap, K. M. K.; Mule, A. S.; Hannagan, R. T.; Matthews, J. E.; Kamat, G. A.; Lee, D. U.; Stevens, M. B.; Nielander, A. C.; et al. On-line Inductively Coupled Plasma Mass Spectrometry Reveals Material Degradation Dynamics of Au and Cu Catalysts during Electrochemical CO2 Reduction. *J. Am. Chem. Soc.* **2025**, *147*, 4079−4088.

(11) Evazzade, I.; Zagalskaya, A.; Alexandrov, V. Revealing Elusive Intermediates of Platinum Cathodic Corrosion through DFT Simulations. *J. Phys. Chem. Lett.* **2022**, *13*, 3047−3052.

(12) Hanselman, S.; Calle-Vallejo, F.; Koper, M. T. M. Computational description of surface hydride phases on Pt(111) electrodes. *J. Chem. Phys.* **2023**, *158* (1), 014703.

(13) Hersbach, T. J. P.; Garcia-Esparza, A. T.; Hanselman, S.; Paredes Mellone, O. A.; Hoogenboom, T.; McCrum, I. T.; Anastasiadou, D.; Feaster, J. T.; Jaramillo, T. F.; Vinson, J.; et al. Platinum hydride formation during cathodic corrosion in aqueous solutions. *Nat. Mater.* **2025**, *24*, 574−580.

(14) Hersbach, T. J. P.; Yanson, A. I.; Koper, M. T. M. Anisotropic etching of platinum electrodes at the onset of cathodic corrosion. *Nat. Commun.* **2016**, *7* (1), 12653.

(15) Arulmozhi, N.; Hersbach, T. J. P.; Koper, M. T. M. Nanoscale morphological evolution of monocrystalline Pt surfaces during cathodic corrosion. *Proc. Natl. Acad. Sci. U. S. A.* **2020**, *117*, 32267−32277.

(16) Elnagar, M. M.; Jacob, T.; Kibler, L. A. Cathodic corrosion of Au in aqueous methanolic alkali metal hydroxide electrolytes: Notable role of water. *Electrochem. Sci. Adv.* **2022**, *2* (6), No. e2100175.

(17) Elnagar, M. M.; Kibler, L. A.; Jacob, T. Structural Evolution of Au Electrodes during Cathodic Corrosion: Initial Stages of Octahedral-Nanocrystal Growth. *J. Electrochem. Soc.* **2022**, *169*, 102509.

(18) Hersbach, T. J. P.; McCrum, I. T.; Anastasiadou, D.; Wever, R.; Calle-Vallejo, F.; Koper, M. T. M. Alkali Metal Cation Effects in Structuring Pt, Rh, and Au Surfaces through Cathodic Corrosion. *ACS Appl. Mater. Interfaces* **2018**, *10*, 39363−39379.

(19) Elnagar, M. M.; Kibler, L. A.; Jacob, T. Effect of Alkali Metal Cations and Trace Metal Impurities on Cathodic Corrosion of Gold Electrode Surfaces. *ChemCatchem* **2024**, *16*, No. e202400526.

(20) Chen, X.; Koper, M. T. M. In Situ EC-AFM Study of the Initial Stages of Cathodic Corrosion of Pt(111) and Polycrystalline Pt in Acid Solution. *J. Phys. Chem. Lett.* **2023**, *14*, 4997−5003.
(21) Duca, M.; Rodriguez, P.; Yanson, A. I.; Koper, M. T. M. Selective Electrocatalysis on Platinum Nanoparticles with Preferential (100) Orientation Prepared by Cathodic Corrosion. *Top. Catal.* **2014**, *57*, 255−264.
(22) Yanson, A. I.; Antonov, P. V.; Yanson, Y. I.; Koper, M. T. M. Controlling the size of platinum nanoparticles prepared by cathodic corrosion. *Electrochim. Acta* **2013**, *110*, 796−800.
(23) Arulmozhi, N.; Jerkiewicz, G. Design and Development of Instrumentations for the Preparation of Platinum Single Crystals for Electrochemistry and Electrocatalysis Research. Part 1: Semi-Automated Crystal Growth. *Electrocatalysis* **2016**, *7*, 507−518.
(24) Guo, L.; Searson, P. C. Anisotropic Island Growth: A New Approach to Thin Film Electrocrystallization. *Langmuir* **2008**, *24*, 10557−10559.
(25) Guo, L.; Searson, P. C. Influence of anion on the kinetics of copper island growth. *Nanoscale* **2010**, *2*, 2431.
(26) Aarts, M.; van Vliet, S.; Bliem, R.; Alarcon-Llado, E. Investigation of copper nanoscale electro-crystallization under directed and non-directed electrodeposition from dilute electrolytes. *CrystEngComm* **2021**, *23*, 3648−3653.
(27) Gosálvez, M. A.; Zubel, I.; Viinikka, E. Wet etching of silicon. In *Handbook of Silicon Based MEMS Materials and Technologies*; Elsevier, 2010; pp. 447−480. DOI: .
(28) Wang, Y.; Garcia-Carrillo, R.; Ren, H. Kinetics and dynamics of atomic-layer dissolution on low-defect Ag. *Chem. Sci.* **2025**, *16*, 1447−1454.
(29) Li, T.; Scully, J. R.; Frankel, G. S. Localized Corrosion: Passive Film Breakdown vs. Pit Growth Stability: Part III. A Unifying Set of Principal Parameters and Criteria for Pit Stabilization and Salt Film Formation. *J. Electrochem. Soc.* **2018**, *165*, C762−C770.
(30) Kuwano, N.; Itakura, M.; Nagatomo, Y.; Tachibana, S. Scanning electron microscope observation of dislocations in semiconductor and metal materials. *J. Electron Microsc. (Tokyo)* **2010**, *59*, S175−S181.
(31) Siegfried, M. J.; Choi, K.-S. Directing the Architecture of Cuprous Oxide Crystals during Electrochemical Growth. *Angew. Chem., Int. Ed.* **2005**, *117*, 3282−3287.
(32) Nagar, M.; Radisic, A.; Strubbe, K.; Vereecken, P. M. The effect of cupric ion concentration on the nucleation and growth of copper on RuTa seeded substrates. *Electrochim. Acta* **2013**, *92*, 474−483.

https://doi.org/10.1021/acs.jpcc.5c05071
J. Phys. Chem. C 2025, 129, 19389−19395